

Spectral Mode Enhancement in Coherent-harmonic Dual-comb Spectroscopy Enables Exceeding 300-fold averaging-time reduction

Wei Long^{1,2,*}, Xinru Cao^{1,2,3}, Xiangze Ma^{1,2,3,4}, Jiaqi Zhou^{1,2,3}, Wenbin He⁵, Dijun Chen^{1,2,3,4,*}

¹Wangzhijiang Innovation Center for Laser, Aerospace Laser Technology and System Department, Shanghai Institute of Optics and Fine Mechanics, Chinese Academy of Sciences, Shanghai 201800, China

²Shanghai Key Laboratory of All Solid-State Laser and Applied Techniques, Shanghai Institute of Optics and Fine Mechanics, Chinese Academy of Sciences, Shanghai 201800, China

³Center of Materials Science and Optoelectronics Engineering, University of Chinese Academy of Sciences, Beijing 100049, China

⁴Hangzhou Institute for Advanced Study, University of Chinese Academy of Sciences, Hangzhou 310024, China

⁵Russell Centre for Advanced Lightwave Science, Shanghai Institute of Optics and Fine Mechanics and Hangzhou Institute of Optics and Fine Mechanics, Chinese Academy of Sciences, Shanghai 201800, China

*longwei20@mailsucas.ac.cn

*djchen@siom.ac.cn

Dual-comb spectroscopy (DCS) is a novel Fourier-transform spectroscopy not relying on mechanical scanning and capable of simultaneously achieving high speed, high spectral resolution, and broad optical bandwidth. Nevertheless, it suffers from low signal-to-noise ratio (SNR) per single acquisition due to the dynamic range limitation of photodetectors imposed by the high-peak-power mode-locked pulses, making coherent averaging an essential means to improve SNR, at the price of compromising the exceptional time resolution and placing more stringent demands on mutual coherence and stability. In this study, a novel approach to enhance SNR by exploiting the spectral mode enhancement mechanism in coherent-harmonic pulses is demonstrated. As a proof-of-concept, two frequency combs with mode spacing of ~ 12.5 MHz, operated at a 20th harmonic repetition rate of ~ 250 MHz, are employed, demonstrating a >300 -fold reduction in averaging time for comparable SNR in conventional DCS. This reduction is expected to be further enhanced through integration with ultra-high repetition rate combs like microresonator combs. This new approach promises both a recovery of the inherent high-speed capability and a mitigation of the coherence-time requirements, thereby making it possible to significantly facilitate subsequent DCS investigations and field deployments.

I. INTRODUCTION

Dual-comb spectroscopy (DCS) is a remarkable novel Fourier-transform spectroscopy technique powered by optical frequency comb (OFC)¹. Over the past decade, it has been increasingly recognized as an important spectroscopic tool in fields that require high speed, broad bandwidth, high frequency resolution, and high frequency accuracy, such as in investigations of physical turbulent environments^{2–6} and chemical and biological dynamic processes^{7–10}. By employing two coherent OFCs with a slight repetition rate difference (Δf_{rep}), and inherently free from mechanical moving parts, DCS can capture an entire interferogram (IGM), yielding a spectrum with a full spectral resolution set by the repetition rate of the combs. The time frame for this capture is as short as $1/\Delta f_{\text{rep}}$, and with large Δf_{rep} configurations, this leads to theoretical temporal resolution reaching microsecond or even nanosecond timescales^{11–13}.

However, in typical practical DCS systems, the high peak power of mode-locked pulses often leads to photodetector saturation or nonlinear response, thus restricting the average power of the combs to a low level. Consequently, given the vast number of comb teeth inherent to broadband spectra, the power per comb tooth is typically

limited to the nanowatt range^{14,15}, ultimately resulting in extremely low SNR per single acquisition, which necessitates coherent averaging or multi-period acquisition to enhance the SNR^{12,15–17}. Unfortunately, the SNR gain achieved through averaging scales proportionally to the square root of the number of averages. For instance, to improve the SNR by a factor of 10, a hundred averages are needed. Obviously, this process not only significantly compromises the exceptional time-resolution of DCS by several orders of magnitude, but also places greater demands on the long-term mutual coherence and stability of the system, which greatly increases the implementation complexity and cost.

To mitigate this issue, one approach involves employing sequential spectrum acquisition using multiple photodetectors¹⁴ or averaging spectral copies instead of IGMs¹⁸. However, the SNR enhancement offered by these two methods has been limited by experimental complexity or sampling bandwidth constraints, demonstrating averaging-time reduction of less than one order of magnitude. Another early approach is to stretch the pulses of the probe comb using a chirped fiber Bragg grating¹⁹. This method can effectively reduce the dynamic range of an IGM; however, it has limited impact on the nonlinearity or saturation induced by pulses,

as the detector's response time significantly exceeds the pulse duration. More recently, the utilization of ~ 1 -GHz-repetition-rate combs^{12,13,20,21} offers higher average power and larger Δf_{rep} . Nevertheless, a ~ 1 -GHz repetition rate had struck a delicate balance between measurement speed and spectral resolution²². A higher repetition rate inherently implies a lower spectral resolution, which limits further increases in repetition rate.

From this perspective, employing frequency combs analogous to certain harmonic mode-locked lasers²³, whose pulse repetition rate (f_{rep}) operates on the harmonics of the laser cavity's fundamental repetition rate, thus possibly featuring a high f_{rep} but a low mode spacing (f_{ms}), may offer a promising avenue. On the one hand, this configuration can enable higher average power within the same dynamic range. On the other hand, the phenomenon that the pulse repetition rate exceeding the mode spacing likely points to an underlying mechanism of the harmonic pulses coherently enhancing their common spectral modes. If this mechanism can be effectively transferred to interferograms in DCS, i.e., generate multiple centerbursts within the time period of $1/\Delta f_{\text{rep}}$ to coherently enhance RF comb modes, it would be possible to achieve the desired SNR gain, thereby potentially refraining from extended IGMs coherent averaging.

Here we find pulse temporal phase modulation (TPM) using electro-optical phase modulator (EOPM) provides an ideal means to realize such combs unaffected by supermode noise³². This TPM has been employed for the comb densification technique^{25–31} based on spectral self-imaging effect²⁴ over the past decade or so, which involves applying periodic TPM to the pulses, inducing evenly spaced "self images" of the original comb lines on the spectrum, thereby densifying the comb. In 2016, N.B. Hébert et al.³³ first introduced this densification technique in DCS and presented an enhanced sub-MHz spectral resolution from a 100-MHz comb, using a pseudo-random binary sequence (PRBS) modulation. In 2024, C. Q.-Galan et al.³⁴ extended this method to 1-GHz gain-switched OFCs, achieving ~ 3.9 MHz resolution. Despite this, both of these two studies primarily focused on the spectral resolution enhancement, merely treating such combs as conventional OFCs with small mode spacing. The underlying harmonic-enhancement mechanism and the descriptions of such special dual-comb have not been elucidated.

In this work, we derived a coherent-harmonic-pulse superposition model in the frequency domain to elucidate this mechanism, and presented the time-domain and equivalent frequency-domain descriptions of two architectures for this special DCS, with a focus on their respective SNR gains. To align with its intuitive physical picture and distinguish it from conventional dual-comb spectroscopy (C-DCS), we term this approach coherent-harmonic-enhanced dual-comb spectroscopy (CH-EDCS). As a proof of concept, we perform transmission spectrum measurements of a hydrogen cyanide ($\text{H}^{13}\text{C}^{14}\text{N}$) gas cell the two proposed ar-

chitectures and, for comparison, a C-DCS architecture. The experiments were based on two commercial 250 MHz combs, which were configured using TPM and a pulse-picking technique⁴¹ to operate at a spectral resolution of 12.5 MHz. As a result, we achieved an SNR gain of up to ~ 18 times per single acquisition, equivalent to a >300 -fold reduction in averaging time, demonstrating the significant potential for SNR enhancement of this approach.

II. PRINCIPLES

In this section, two DCS architectures for this CH-EDCS concept are studied: one termed C-H-OFC, employing a coherent-harmonic optical frequency comb (H-OFC) realized by TPM and a conventional optical frequency comb (C-OFC); the other termed H-H-DCS, employing two H-OFCs. For clarity, we use a harmonic number of $m = 4$ and a TPM sequence of $[\pi, 0, 0, 0]$ as illustrative examples.

A. C-H-DCS

As illustrated in Figs. 1 (c) and (d), C-H-DCS utilizes a H-OFC whose repetition rate is approximately equal to 4 times of the repetition rate of the C-OFC (or, more generally, any integer multiple m). The pulses of comb 1, after stepping across the first pulse of the H-OFC, subsequently scan its 2nd to 4th pulses, thus generating four centerbursts instead of a single one on the interferogram within the same time period. Additionally, according to the principle of linear optical sampling^{35,36}, the expression for the interference intensity can be written as

$$I(n) \sim \sum_n \langle |E_1(t - n\tau)| |E_2(t)| \cos(\Delta\omega_c t + \phi_{TPM}) \rangle, \quad (1)$$

where $E_1(t)$, $E_2(t)$ represents the pulses' electric field envelopes; n denotes the pulse pair number; τ denotes the time delay induced by the repetition rate difference; and ϕ_{TPM} represents the phase difference introduced by the TPM. For each centerburst, the ϕ_{TPM} is constant. Consequently, the TPM imposed on the pulses of H-OFC is finally mapped onto the four centerbursts.

The spectral behavior of the H-OFC and the interferogram with 4 centerbursts can be elucidated through the interference of the harmonic pulses. The original pulse train is decomposed into a collection of four sub-harmonic pulse trains, each with a period of $1/f_{\text{ms}}$ ($1/\Delta f_s$ for the interferogram) and corresponding to a sub-spectrum with mode spacing of f_{ms} . According to the linear property of the Fourier transform, the spectrum of the H-OFC or the interferogram at frequency ω_j is a vector superposition of the 4 sub-modes at that frequency, given by $E_j = \sum_{k=1}^4 a_0 \exp(\omega_j t + \phi_{k,j})$, where a_0 is the amplitude of the sub-modes. Considering the influence of the

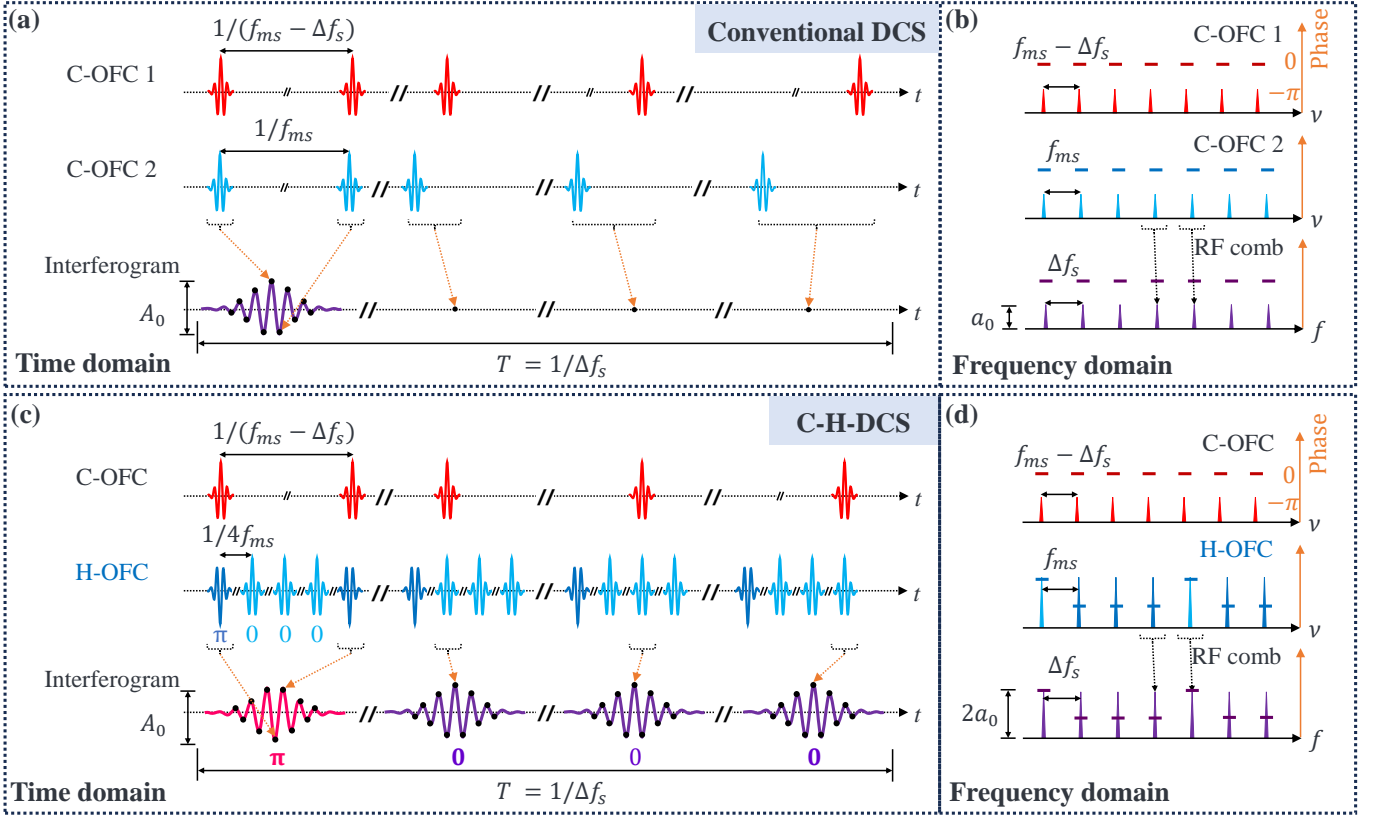


Fig. 1: Concepts of conventional DCS (C-DCS) and C-H-DCS. **(a)** Time-domain description of C-DCS. The pulse train (red) of comb 1 progressively steps across another pulse train (blue) with a slight repetition rate difference Δf_s , generating an interferogram with a single centerburst in a period of $1/\Delta f_s$. When the temporal interval between the two pulses is large, effective interference does not occur. **(b)** The equivalent frequency-domain description of the C-DCS. The beating of two combs produces an RF comb in the radio-frequency domain. **(c)** Time-domain description of the C-H-DCS. The pulse of the conventional optical frequency comb (C-OFC) with a pulse repetition rate of $f_{ms} - \Delta f_s$, steps across the four pulses of the coherent-harmonic optical frequency comb (H-OFC), which have phases of $[\pi, 0, 0, 0]$ and a pulse repetition rate of $4f_{ms}$. This generates four centerbursts within an interferogram period of $1/\Delta f_s$, which inherit the $[\pi, 0, 0, 0]$ phases. **(d)** The equivalent frequency-domain description of the C-H-DCS. Two combs with mode spacing of $f_{ms} - \Delta f_s$ and f_{ms} respectively beat together, producing an RF comb in the radio-frequency domain. This RF comb inherits the $[0, -\pi, -\pi, -\pi]$ periodic multilevel phase profile of the H-OFC and exhibits twice the line amplitude compared to the C-DCS.

relative time delay among these harmonic trains and the TPM, the phase spectrum of the k th-sub-spectrum can be expressed as

$$\phi_{k,j} = -\omega_j t_k + \phi_{TPM,k} = -\frac{j}{4}(k-1) \cdot 2\pi + \phi_{TPM,k}. \quad (2)$$

The first term in the formula, $-\omega_j t_k$, arises from the contribution of the Fourier time shift, where $\omega_j = j \cdot 2\pi f_{ms}$ is the angular frequency of the j th mode, $t_k = (k-1)/4f_{ms}$ is the time delay of k th-sub-harmonic pulse train relative to the first sub-harmonic pulse train; the second term, $\phi_{TPM,k}$, is the phase shift added to the k th-train through the TPM. The superposition process and results are illustrated in Fig. 2, with vector sum $E_j = 2a_0 \exp(\omega_j t + \varphi_j)$ where φ_j is a periodic sequence $[-\pi, -\pi, -\pi, 0]$. This indicates that the spectrum of the original pulse train has

the same mode spacing but twice the amplitude of the sub-spectrum, and exhibits a periodic multilevel phase spectrum of $[-\pi, -\pi, -\pi, 0]$.

Thus, an SNR gain of 2 can be achieved without coherent averaging 4 IGMs (spanning a total time of $4/\Delta f_s$ in the C-DCS). For a more general case, the number 4 in the aforementioned equations corresponds to m , and the corresponding SNR gain is \sqrt{m} . Moreover, it is worth noting that if a flat gain is required, an equation in the quadratic function form indicated by the so-called "Talbot condition"³⁷ can be used, which is expressed as

$$\phi_{n;s,m} = \pi \frac{s}{m} k^2 (\text{mod } 2\pi), \quad (3)$$

where s, m are mutually prime integer numbers, and k is the pulse number. Correspondingly, the periodic mul-

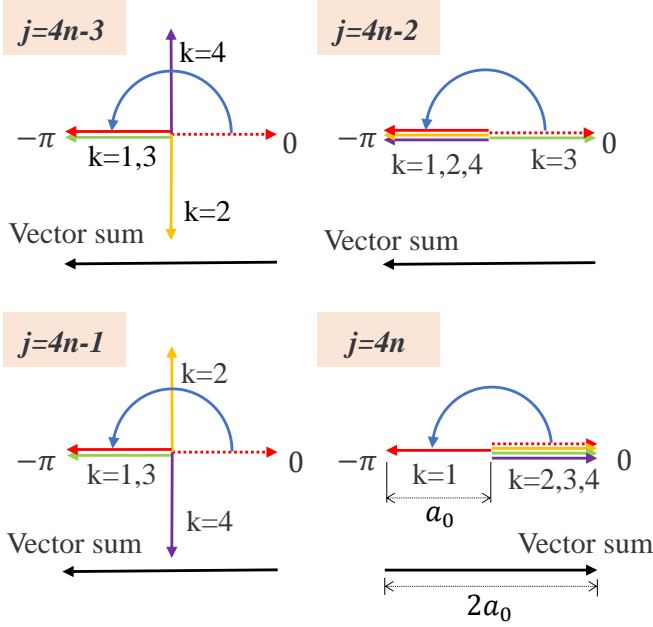


Fig. 2: Illustration of the process of the spectral mode enhancement by the harmonic pulse trains in the frequency domain. The j represents the spectral mode index (derived from $\omega_j = j \cdot 2\pi f_{ms}$). The colored linear arrows with indexes of $k = 1, 2, 3, 4$ represent the mode vectors from the k th-sub-harmonic pulse train at the frequency of ω_j , while the blue rotating arrows indicate the temporal phase modulation (TPM), which rotates all the modes of the 1st-sub-harmonic pulse train ($k = 1$) by π . In the absence of this TPM, only the modes of $j = 4n$ ($n \in \mathbb{Z}^+$) will be present, while the remaining modes will undergo destructive interference, consistent with conventional expectation. The black arrows represent the total mode vectors after superposition, which have twice the amplitude of the sub-modes and exhibit a periodic phase profile of $[-\pi, -\pi, -\pi, 0]$.

tilevel phase profile of the total spectrum is $\varphi_{k;p,q} = -\pi \frac{p}{q} j^2 (\text{mod } 2\pi)$, where $q = m$, j is the mode number, and $p \neq s$ in general. Whereas, if a reference channel for spectral normalization in DCS configuration is available, the majority of periodic signal can be set.

B. H-H-DCS

As illustrated in Fig. 3, C-H-DCS utilizes two H-OFCs with pulse repetition rates of $4f_{ms}$ and $4(f_{ms} - \Delta f_s)$. In the time domain, similar to a C-DCS with the same repetition rate difference of $4\Delta f_s$, this architecture generates 4 centerbursts within a time period of $1/\Delta f_s$. Due to this repetition rate difference, the phase-inverted pulses in the two pulse trains gradually slip relative to each other, resulting in distinct in-pulse-pair phase configurations: $[\pi, 0, 0, 0] - [\pi, 0, 0, 0]$, $[0, \pi, 0, 0] - [\pi, 0, 0, 0]$,

$[0, 0, \pi, 0] - [\pi, 0, 0, 0]$, and $[0, 0, 0, \pi] - [\pi, 0, 0, 0]$, respectively, in the time domain regions corresponding to the four centerbursts. Consequently, the ϕ_{TPM} in Eq. 1, is constantly 0 for the first centerburst; while for the other three centerbursts, the values are periodic $[\pi, \pi, 0, 0]$, $[\pi, 0, \pi, 0]$, and $[\pi, 0, 0, \pi]$, respectively. These time-varying phases (related to the pulse pair index, i.e., time) increase the oscillation frequency of the interference electric field, shifting the 2nd to 4th centerbursts to higher-order components, which can be filtered out by an electronic low-pass filter in practical implementation. In fact, these high-order components correspond to spectral copies generated by the heterodyning of teeth from comb 1 with non-nearest teeth from comb 2 in the spectrum, as detailed in Supplement 1.

Thus, the IGM exhibits only one fundamental centerburst within a time period of $1/\Delta f_s$, similar to that in the C-DCS. Distinctly, the fundamental centerburst originates from the contribution of 4 times the number of pulse pairs, whose interference intensity is given by $I'(n) \sim \sum_{n=1}^{4n_0} \langle |E_1(t - n\tau/4)| |E_2(t)| \cos \Delta\omega_c t \rangle$, where n_0 is the number of pulse pairs contributing to the centerburst in the C-DCS illustrated in Fig. 1(a). Consequently, following convolution with the detector response and low-pass filtering, the amplitude of this centerburst is also enhanced by a factor of 4.

In the frequency domain, two H-OFCs with 2-fold mode amplitude enhancement and periodic multilevel phase spectra of $[-\pi, -\pi, -\pi, 0]$, beat together to yield an RF comb. Since the amplitude of a heterodyne beat note is the product of the amplitudes of the two beating components, and the phase is the phase difference between them, the modes of this RF comb therefore exhibit a 4-fold enhancement in amplitude and possess a uniform phase, which precisely corresponds to the single fundamental centerburst with a 4-fold increase in amplitude in the time domain.

Thus, this architecture leads to a 4-fold SNR gain. For a more general case, this number 4 corresponds to m , and is equivalent to an SNR gain brought by coherent averaging spanning a total time of m^2 -fold.

Interestingly, the aforementioned IGM characteristics can be changed (the SNR gain is not changed) when the two TPM signals use the quadratic form described in Eq. 3 with the same m but different s values. The generated RF comb can exhibit quadratic periodic multilevel phase profiles of $-\pi \frac{p_1 - p_2}{m} j^2$. According to the temporal self-imaging effect^{30,38}, the fundamental centerburst on the IGM will then be redistributed, similar to that in C-H-DCS.

III. EXPERIMENT

As a proof of concept, we performed experiments with the three architectures using two commercially available 250-MHz fiber mode-locked combs at 1550 nm (Menlo Systems, 250-ULN and 250-WG-PM), as sketched in Fig.

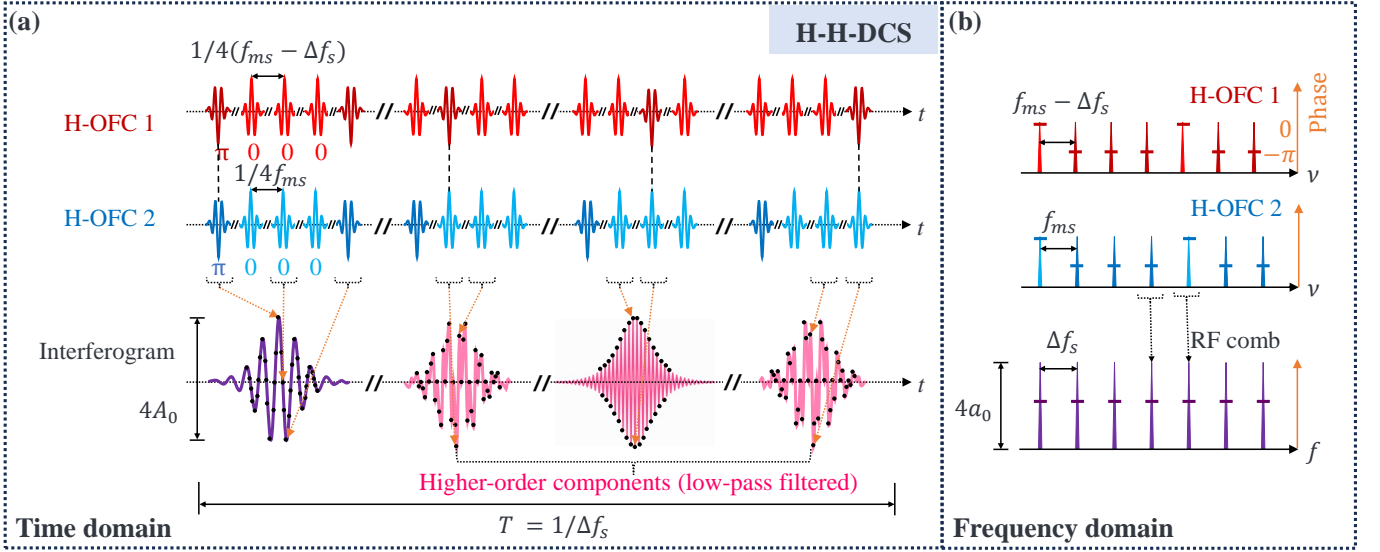


Fig. 3: Concept of H-H-DCS. (a) Time-domain description of the H-H-DCS. The H-OFC 1 and H-OFC 2 emit two pulse trains with repetition rate of $4(f_{ms} - \Delta f_s)$ and $4f_{ms}$ respectively, both with pulse phases of $[\pi, 0, 0, 0]$. Interference of the two pulse trains within a time period of $1/\Delta f_s$ produces four distinct centerbursts: one at the fundamental oscillation frequency (purple), exhibiting a 4-fold amplitude enhancement over conventional dual-comb spectroscopy (C-DCS); and three additional centerbursts at higher-order frequencies (pink), which are suppressed by low-pass filtering in practical implementations. (b) The equivalent frequency-domain description of the H-H-DCS. Two H-OFCs with mode spacing of $f_{ms} - \Delta f_s$ and f_{ms} respectively beat together, producing an RF comb in the radio-frequency domain which has a uniform phase profile and exhibits four times the line amplitude compared to the C-DCS. Note that, the uniform phase profile requires the phase profiles of the two H-OFCs to be accurately aligned.

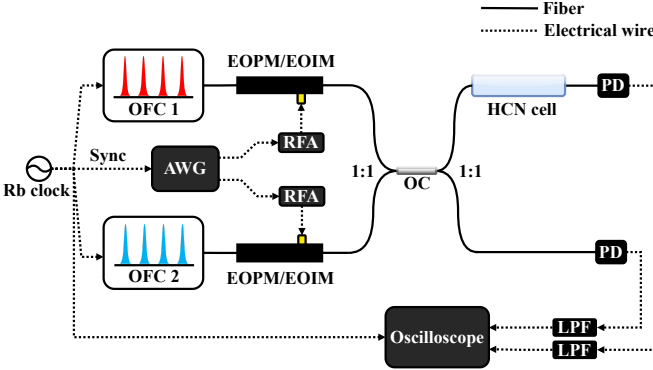


Fig. 4: Sketch of experimental setup. Rb clock: rubidium clock; OFC: optical frequency comb; AWG: arbitrary waveform generator; RFA: RF amplifiers; EOPM/EOIM: electro-optical phase/intensity modulator; OC: optical coupler; PD: photodetector; LPF: low-pass filter.

4 (implementation details are available in Supplementary Fig. S1). The TPM periods were set to 20 times the pulse period in the C-H-DCS and H-H-DCS experiments, yielding a harmonic number of 20 and a spectral resolution of 12.5 MHz. The TPM is executed by an EOPM with 10-GHz bandwidth. Given a lack of high-quality C-

OFCs operating at a repetition rate of 12.5 MHz, and a need for control over variables such as pulse energy and power, the two 12.5 MHz C-OFCs are emulated by implementing the pulse-picking technique^{39,41} with a picking factor of 1/20 applied to the original pulse trains, through electro-optic intensity modulators (EOIMs) also with 10-GHz bandwidth. An arbitrary waveform generator (AWG, Keysight-M8190A) with a bandwidth of 4 GHz and operating at a sampling rate of 10 GHz, generated modulation signals for these modulators. Specifically, the EOIMs were driven by periodic square-wave signals with a 3% duty cycle (below 5% to ensure better suppression of adjacent pulses) and repetition frequency of 12.5 MHz, while the electro-optic phase modulators (EOPMs) were driven by the quadratic form referenced in Eq. 3, using $m = 20$ and $s = 1$ as parameters. Two RF amplifiers (Mini-Circuits ZHL-10M4G21W0+) amplified the modulation signals to an appropriate voltage level required for modulator operation.

Moreover, the two OFCs operated at repetition rates of 250 MHz and 249.98 MHz with a $\Delta f_{rep} = 20$ kHz, and carrier-envelope offset frequencies (f_{ceo}) of 20 MHz and 33.5 MHz, respectively. To ensure long-term stability of the system, these f_{ceo} and f_{rep} were simply phase-locked to a rubidium atomic clock, with which the AWG was also timing synchronized (variable delay lines or RF phase shifters can be employed to align the

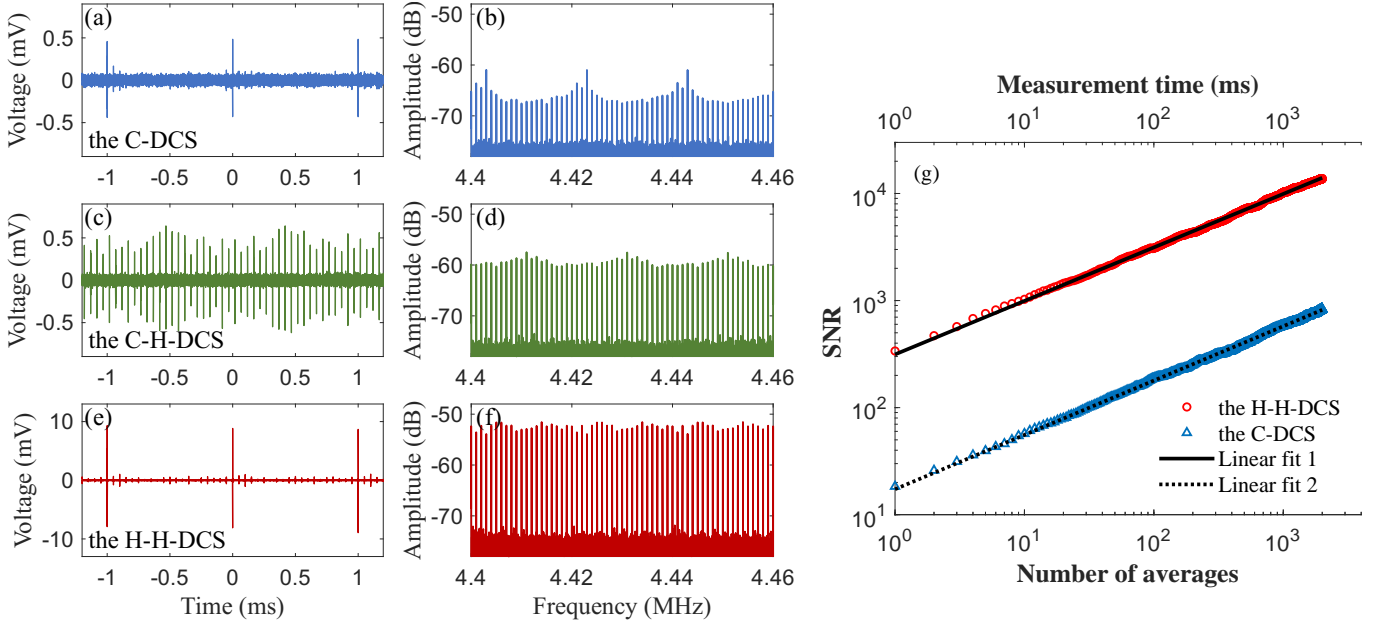


Fig. 5: Comparison of interferograms (IGMs) and signal-to-noise ratio (SNR) for the three architectures. (a) IGMs of the C-DCS and (b) its spectrum (partial). The centerburst repetition rate is 1 kHz, matching the spectral line spacing, as expected for conventional DCS. The spectrum exhibits a 20 kHz amplitude periodicity, with prominent lines attributed to the non-ideal extinction ratio of the EOIMs³⁹. (c) IGMs of the C-H-DCS and (d) its spectrum. The centerburst repetition rate is observed at 20 kHz, a 20th harmonic of its line spacing of 1 kHz, corresponding to the average mode amplitude in the spectrum increasing to > -60 dB. (e) IGMs of the H-H-DCS and (f) its spectrum. The centerburst repetition rate and the line spacing are both observed to be 1 kHz. The amplitude of the centerbursts is significantly increased to a value approaching 20 mVpp, corresponding to the spectral mode amplitude increased to close to -50 dB. (g) Evolution of time-domain SNR for the H-H-DCS and the C-DCS with the number of averages. On the log-log scale, the linear fitting models of the two datasets are given by $fit\ 1 = 0.4997(4)x + 2.497(1)$ and $fit\ 2 = 0.5075(4)x + 1.238(1)$. The slopes, approximating 0.5, indicate that the SNR is proportional to the square root of the number of averages, consistent with the principle of coherent averaging. The time-domain SNR is defined as the ratio of the centerburst amplitude to the standard deviation of a segment away from the centerburst⁴⁰.

optical pulses and modulation signals). Additionally, the high degree of mutual coherence essential for DCS was retrieved through the optical referencing and post-treatment techniques^{19,42,43}, which can be regarded as an original digital version of the adaptive scheme⁴⁴.

For the DCS experiments, an $H^{13}C^{14}N$ gas cell (Wavelength References, HCN-13-10), with a nominal pressure of approximately 10 Torr and a path length of 16.5 cm, was selected as a representative sample. The two modulated combs were mixed and subsequently split into measurement and reference beams using a 50/50 coupler. The measurement beam traversed the $H^{13}C^{14}N$ gas cell before detection by a biased detector (Thorlabs, DET01CFC), while the reference beam was directly detected. This reference channel is crucial for eliminating comb tooth fluctuations arising from the uneven gain caused by the error in ϕ_{TPM} . IGMs from both detectors were low-pass filtered (6 MHz @3 dB) and simultaneously digitized by an oscilloscope at a sampling rate of 31.25 MS/s. The optical power incident on the detector in the measurement beam was 11.9 μW , 119 μW , and 223 μW

for the C-DCS, the C-H-DCS, and the H-H-DCS, respectively, limited by filter bandwidth and amplifier limitations (Supplementary Fig. S1).

IV. RESULTS AND DISCUSSION

A. Features of Interferograms

Figure 5(a-f) displays the IGMs generated in the three architectures and their corresponding spectra after post treatment. As anticipated, the centerburst repetition rate in the C-H-DCS is 20 times higher than that of the C-DCS, while maintaining the same spectral mode spacing and achieving an average enhancement of the mode amplitude by approximately 7 dB ($10\lg\sqrt{20}$).

As for the H-H-DCS, the centerburst amplitude is approximately 20 times greater than that in the C-DCS. This corresponds to an average enhancement of the mode amplitude by approximately 13 dB ($10\lg 20$) in the spectrum. The noise floor in the spectrum also increases by

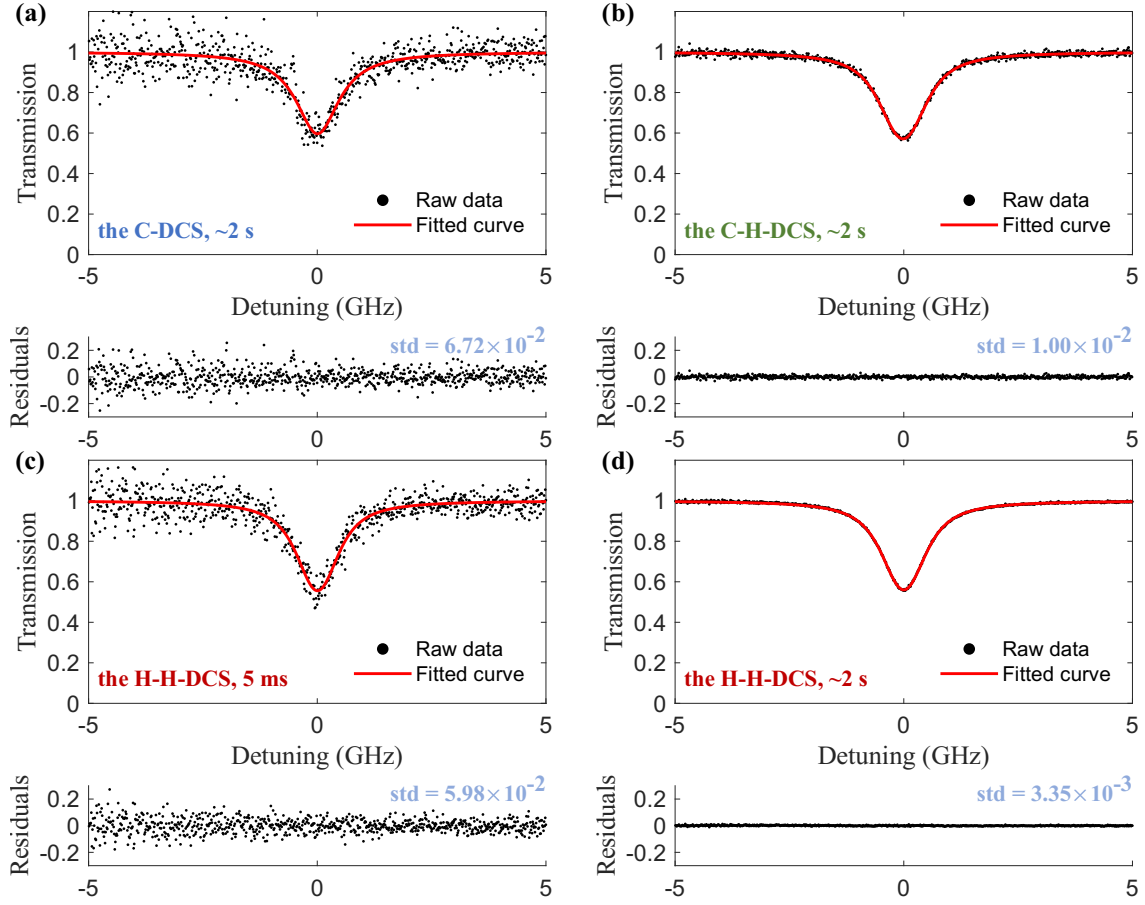


Fig. 6: Example $\text{H}^{13}\text{C}^{14}\text{N}$ spectra relative to the center frequency of 193.5449 THz (1548.9555 nm) at a spectral resolution of 12.5 MHz, along with the corresponding weighted Voigt profile fits. **(a)** Recorded in 1.999 s (1999 averages) in the C-DCS. **(b)** Recorded in 1.999 s in the C-H-DCS. **(c)** Recorded in 5 ms (5 averages) in the H-H-DCS. **(d)** Recorded in 1.999 s in the H-H-DCS. The standard deviations of the four fitting residuals were calculated, with the residual noise in **(d)** is reduced by a factor of ~ 20 compared to that in **(a)**.

about 2 dB, potentially due to higher relative intensity noise. Furthermore, in addition to the primary centerbursts, the IGMs of the H-H-DCS also show weak centerbursts with a 1/20 ms interval, which is attributed to imperfect transfer of the oscillation frequency due to errors in the driving signal levels. The mode superposition of these weak centerbursts caused the unflatness on the RF comb, i.e., an amplitude modulation with a period of 20 kHz, as shown in Figs. 5(e) and (f). Details regarding the higher-order components are presented in Supplementary Fig. S3.

A potential misconception might arise that the amplified centerburst amplitude necessitates a larger detector dynamic range. In fact, as mentioned in the principle section, this is a superposition resulting from the convolution of the additional pulse pairs due to low-pass filtering.

B. Time-domain Signal-to-noise Ratio

The evolution of the time-domain SNR for the H-H-DCS and the C-DCS with respect to the number of averages (or measurement time) is calculated in Fig. 5(g). The x-axis intercepts of the two linear fits exhibit a difference of 2.5575, indicating that this new architecture reduces the required number of averages or measurement time to achieve the same SNR by a factor of 361 (1/361 of the original). The y-axis intercepts show a difference of 1.259, indicating an approximate 18-fold enhancement in SNR for the same number of averages. These findings are consistent with the expected performance for a setup with $m = 20$.

C. Transmission Spectrum

The enhancement in time-domain SNR is manifested in the transmission spectrum. Fig. 6 presents the acquired transmission spectra around the P7 absorption line of

$\text{H}^{13}\text{C}^{14}\text{N}$ using the three architectures, with a spectral point spacing of 12.5 MHz. Both architectures, particularly the H-H-DCS, demonstrate significantly reduced residual levels within the same measurement time compared to the C-DCS. Furthermore, the standard deviations of the fitting residual observed in a 5-ms measurement using H-H-DCS are comparable to those in a ~ 2 -s measurement using C-DCS.

D. Discussion

The proof-of-concept results presented in this work can be further improved by combining with ultrahigh-repetition-rate comb sources, or when probing with finer spectral resolution. For example, when combined with 22-GHz microresonator combs⁴⁵ and operating at a spectral resolution of 500 MHz, compared to conventional DCS with the same resolution, an exceeding 1500-fold averaging-time reduction is expected. Furthermore, integrated lithium niobate electro-optic modulators operating at CMOS-compatible voltages may facilitate this implementation⁴⁶.

In wavelength regions where mature EOPMs are not readily available, this approach may be achieved using nonlinear means. For example, under second-harmonic generation⁴⁷, a temporal pulse-phase profile of $[0, 0, 0, \pi/2]$ is anticipated to transform to the desired $[0, 0, 0, \pi]$, and a profile of $\pi \frac{s}{2m} k^2$ is anticipated to transform to the desired $\pi \frac{s}{m} k^2$.

For field-deployed DCS, the mitigation in coherence time inherently offers significant advantages. Further possible combination with ultra-low-noise optical frequency combs, such as the compact monolithic solid-state design⁴⁸ that provides a ~ 100 Hz linewidth in a quasi-free-running state, complex and sophisticated locking systems may be greatly simplified. Moreover, the decoupling of the centerburst repetition rate and the Δf_{rep} (i.e. Δf_s) also overcomes the limitation on the noise tracking bandwidth of post-treatment algorithms in free-running DCS, which was previously limited to half the IGM repetition rate (i.e. $\Delta f_{\text{rep}}/2$)^{43,49}, a restriction that can be roughly attributed to the fact that in conventional DCS, only a single centerburst within each IGM provides effective sampling.

Finally, it is worth emphasizing that the essence of this spectral mode enhancement lies in enabling the optical frequency comb or combs to output multiple special

harmonic pulse trains with the same carrier-envelope offset frequency, but different carrier-envelope phases (nonlinear slip), thereby enhancing the majority of the mode sets rather than enhancing a few and suppressing others. The scheme demonstrated in this paper, which employs TPM based on EOPMs outside the cavity, may not be the only method to achieve this SNR enhancement. For example, in some parametrically driven Kerr soliton microresonators, two soliton states with opposite phases owing to the Z_2 -symmetry have been observed⁵⁰, and a soliton sequence with random phase bits of $[0, 0, \pi, 0]$ has been demonstrated⁵¹.

V. CONCLUSION

In summary, this work has opened up another effective way to enhance the SNR in DCS beyond coherent averaging, through coherent superposition of harmonic pulses. In our proof-of-concept experiments based on temporal phase modulation, we have successfully demonstrated an ~ 18 -fold SNR enhancement in a single acquisition, which is equivalent to an SNR gain achieved by coherent averaging over >300 periods in conventional DCS. This approach avoids the need for long-time averaging, thus enabling recovery of the inherent excellent temporal resolution of DCS and promising to relax stringent requirements on coherence time and stability of DCS systems. This could potentially have significant implications for future DCS research and applications.

Acknowledgments

This work was supported by National Key Research and Development Program of China under Grant2020YFC2200300. The authors thank Prof. Tang Li for providing the Menlo-250-WG-PM, Yatan Xiong for lending the EDFA, and Hao Li, Yinnan Chen, Zheng Liu, Yujia Ji, and Yanan Qu for their assistance with certain details.

Disclosures

The authors declare no conflicts of interest.

Data availability

Data underlying the results presented in this paper are not publicly available at this time but may be obtained from the authors upon reasonable request.

Supplemental document

See Supplement 1 for supporting content.

-
- [1] Fortier, T. & Baumann, E. 20 years of developments in optical frequency comb technology and applications. *Communications Physics* **2**, 1–16 (2019).
 - [2] Rieker, G. B. *et al.* Frequency-comb-based remote sensing of greenhouse gases over kilometer air paths. *Optica*

1, 290 (2014).

- [3] Sinclair, L. C. *et al.* Optical phase noise from atmospheric fluctuations and its impact on optical time-frequency transfer. *Physical Review A* **89**, 023805 (2014).
- [4] Coburn, S. *et al.* Regional trace-gas source attribution

- using a field-deployed dual frequency comb spectrometer. *Optica* **5**, 320–327 (2018).
- [5] Yun, D. *et al.* Spatially resolved mass flux measurements with dual-comb spectroscopy. *Optica* **9**, 1050 (2022).
 - [6] Han, J.-J. *et al.* Dual-comb spectroscopy over a 100 km open-air path. *Nature Photonics* 1–8 (2024).
 - [7] Klocke, J. L. *et al.* Single-shot sub-microsecond mid-infrared spectroscopy on protein reactions with quantum cascade laser frequency combs. *Analytical chemistry* **90**, 10494–10500 (2018).
 - [8] Pinkowski, N. H. *et al.* Dual-comb spectroscopy for high-temperature reaction kinetics. *Measurement Science and Technology* **31**, 055501 (2020).
 - [9] Norahan, M. J. *et al.* Microsecond-Resolved Infrared Spectroscopy on Nonrepetitive Protein Reactions by Applying Caged Compounds and Quantum Cascade Laser Frequency Combs. *Analytical Chemistry* **93**, 6779–6783 (2021).
 - [10] Westberg, J. *et al.* Urban open-air chemical sensing using a mobile quantum cascade laser dual-comb spectrometer. *APL Photonics* **8**, 120803 (2023).
 - [11] Abbas, M. A. *et al.* Time-resolved mid-infrared dual-comb spectroscopy. *Scientific Reports* **9**, 17247 (2019).
 - [12] Hoghooghi, N., Cole, R. K. & Rieker, G. B. 11- μ s time-resolved, continuous dual-comb spectroscopy with spectrally filtered mode-locked frequency combs. *Applied Physics B* **127**, 17 (2021).
 - [13] Long, D. A. *et al.* Nanosecond time-resolved dual-comb absorption spectroscopy. *Nature Photonics* **18**, 127–131 (2024).
 - [14] Newbury, N. R., Coddington, I. & Swann, W. Sensitivity of coherent dual-comb spectroscopy. *Optics Express* **18**, 7929–7945 (2010).
 - [15] Coddington, I., Newbury, N. & Swann, W. Dual-comb spectroscopy. *Optica* **3**, 414–426 (2016).
 - [16] Keilmann, F., Gohle, C. & Holzwarth, R. Time-domain mid-infrared frequency-comb spectrometer. *Optics Letters* **29**, 1542 (2004).
 - [17] Chen, Z., Yan, M., Hänsch, T. W. & Picqué, N. A phase-stable dual-comb interferometer. *Nature Communications* **9**, 3035 (2018).
 - [18] Walsh, M., Guay, P. & Genest, J. Unlocking a lower shot noise limit in dual-comb interferometry. *APL Photonics* **8**, 071302 (2023).
 - [19] Deschênes, J.-D., Giaccarri, P. & Genest, J. Optical referencing technique with CW lasers as intermediate oscillators for continuous full delay range frequency comb interferometry. *Optics Express* **18**, 23358 (2010).
 - [20] Bao, C. *et al.* Architecture for microcomb-based GHz-mid-infrared dual-comb spectroscopy. *Nature Communications* **12**, 6573 (2021).
 - [21] Ling, L. *et al.* Practical GHz single-cavity all-fiber dual-comb laser for high-speed spectroscopy. *Light: Science & Applications* **14**, 133 (2025).
 - [22] Hoghooghi, N. *et al.* Broadband 1-GHz mid-infrared frequency comb. *Light: Science & Applications* **11**, 264 (2022).
 - [23] He, W., Pang, M., Menyuk, C. R. & Russell, P. S. J. Sub-100-fs 1.87 GHz mode-locked fiber laser using stretched-soliton effects. *Optica* **3**, 1366–1372 (2016).
 - [24] Azaña, J. Spectral Talbot phenomena of frequency combs induced by cross-phase modulation in optical fibers. *Optics Letters* **30**, 227 (2005).
 - [25] Caraquitená, J., Beltrán, M., Llorente, R., Martí, J. & Muriel, M. A. Spectral self-imaging effect by time-domain multilevel phase modulation of a periodic pulse train. *Optics Letters* **36**, 858 (2011).
 - [26] Beltran, M., Caraquitená, J., Llorente, R. & Martí, J. Reconfigurable Multiwavelength Source Based on Electrooptic Phase Modulation of a Pulsed Laser. *IEEE Photonics Technology Letters* **23**, 1175–1177 (2011).
 - [27] Malacarne, A. & Azaña, J. Discretely tunable comb spacing of a frequency comb by multilevel phase modulation of a periodic pulse train. *Optics Express* **21**, 4139 (2013).
 - [28] de Chatellus, H. G., Cortés, L. R. & Azaña, J. Arbitrary energy-preserving control of the line spacing of an optical frequency comb over six orders of magnitude through self-imaging. *Optics Express* **26**, 21069–21085 (2018).
 - [29] Li, X.-Z. & Azana, J. On Mode-Spacing Division of a Frequency Comb by Temporal Phase Modulation. *IEEE Journal of Selected Topics in Quantum Electronics* **25**, 1–10 (2019).
 - [30] Romero Cortés, L., Maram, R., Guillet de Chatellus, H. & Azaña, J. Arbitrary Energy-Preserving Control of Optical Pulse Trains and Frequency Combs through Generalized Talbot Effects. *Laser & Photonics Reviews* **13**, 1900176 (2019).
 - [31] Li, X.-Z., Seghilani, M., Maram, R., Cortes, L. R. & Azana, J. Ultra-Dense CEO-Stabilized Broadband Optical Frequency Comb Generation Through Simple, Programmable, and Lossless 1000-Fold Frequency-Spacing Division. *IEEE Photonics Journal* **11**, 1–12 (2019).
 - [32] Gee, S., Quinlan, F., Ozharar, S. & Delfyett, P. J. Correlation of supermode noise of harmonically mode-locked lasers. *JOSA B* **24**, 1490–1497 (2007).
 - [33] Hébert, N. B., Michaud-Belleau, V., Magnan-Saucier, S., Deschênes, J.-D. & Genest, J. Dual-comb spectroscopy with a phase-modulated probe comb for sub-MHz spectral sampling. *Optics Letters* **41**, 2282 (2016).
 - [34] Quevedo-Galán, C., Rosado, A., Pérez-Serrano, A., Tijero, J. M. G. & Esquivias, I. Dual-comb spectroscopy with enhanced resolution by pseudorandom phase modulation of gain-switched optical pulses. *Journal of Lightwave Technology* 1–9 (2024).
 - [35] Schiller, S. Spectrometry with frequency combs. *Optics Letters* **27**, 766 (2002).
 - [36] Coddington, I., Swann, W. C. & Newbury, N. R. Coherent linear optical sampling at 15 bits of resolution. *Optics Letters* **34**, 2153 (2009).
 - [37] Cortés, L. R., de Chatellus, H. G. & Azaña, J. On the generality of the Talbot condition for inducing self-imaging effects on periodic objects. *Optics Letters* **41**, 340–343 (2016).
 - [38] Maram, R., Van Howe, J., Li, M. & Azaña, J. Noiseless intensity amplification of repetitive signals by coherent addition using the temporal Talbot effect. *Nature Communications* **5**, 5163 (2014).
 - [39] Vieira, F. S., Cruz, F. C., Plusquellic, D. F. & Diddams, S. A. Tunable resolution terahertz dual frequency comb spectrometer. *Optics Express* **24**, 30100 (2016).
 - [40] Friedlein, J. T. *et al.* Dual-comb photoacoustic spectroscopy. *Nature Communications* **11**, 3152 (2020).
 - [41] Canella, F. *et al.* Low-repetition-rate optical frequency comb. *Optica* **11**, 1 (2024).
 - [42] Hébert, N. B. *et al.* Self-corrected chip-based dual-comb spectrometer. *Optics Express* **25**, 8168 (2017).
 - [43] Hébert, N. B., Michaud-Belleau, V., Deschenes, J.-D. & Genest, J. Self-Correction Limits in Dual-Comb Interfer-

- ometry. *IEEE Journal of Quantum Electronics* **55**, 1–11 (2019).
- [44] Ideguchi, T., Poisson, A., Guelachvili, G., Picqué, N. & Hänsch, T. W. Adaptive real-time dual-comb spectroscopy. *Nature Communications* **5**, 3375 (2014).
- [45] Suh, M.-G., Yang, Q.-F., Yang, K. Y., Yi, X. & Vahala, K. J. Microresonator soliton dual-comb spectroscopy. *Science* **354**, 600–603 (2016).
- [46] Wang, C. *et al.* Integrated lithium niobate electro-optic modulators operating at CMOS-compatible voltages. *Nature* **562**, 101–104 (2018).
- [47] Jones, D. J. Carrier-Envelope Phase Control of Femtosecond Mode-Locked Lasers and Direct Optical Frequency Synthesis. *Science* **288**, 635–639 (2000).
- [48] Shoji, T. D. *et al.* Ultra-low-noise monolithic mode-locked solid-state laser. *Optica* **3**, 995 (2016).
- [49] Burghoff, D., Han, N. & Shin, J. H. Generalized method for the computational phase correction of arbitrary dual comb signals. *Optics Letters* **44**, 2966 (2019).
- [50] Moille, G. *et al.* Parametrically driven pure-Kerr temporal solitons in a chip-integrated microcavity. *Nature Photonics* **18**, 617–624 (2024).
- [51] Englebert, N. *et al.* Parametrically driven Kerr cavity solitons. *Nature Photonics* **15**, 857–861 (2021).

Supplement 1: Spectral Mode Enhancement in Coherent-harmonic Dual-comb Spectroscopy Enables Exceeding 300-fold Averaging Time Reduction

Wei Long^{1,2,*}, Xinru Cao^{1,2,3}, Xiangze Ma^{1,2,3,4}, Jiaqi Zhou^{1,2,3}, Wenbin He⁵, Dijun Chen^{1,2,3,4,*}

¹Wangzhijiang Innovation Center for Laser, Aerospace Laser Technology and System Department, Shanghai Institute of Optics and Fine Mechanics, Chinese Academy of Sciences, Shanghai 201800, China

²Shanghai Key Laboratory of All Solid-State Laser and Applied Techniques, Shanghai Institute of Optics and Fine Mechanics, Chinese Academy of Sciences, Shanghai 201800, China

³Center of Materials Science and Optoelectronics Engineering, University of Chinese Academy of Sciences, Beijing 100049, China

⁴Hangzhou Institute for Advanced Study, University of Chinese Academy of Sciences, Hangzhou 310024, China

⁵Russell Centre for Advanced Lightwave Science, Shanghai Institute of Optics and Fine Mechanics and Hangzhou Institute of Optics and Fine Mechanics, Chinese Academy of Sciences, Shanghai 201800, China

*longwei20@mailsucas.ac.cn

*djchen@siom.ac.cn

(Dated: April 29, 2025)

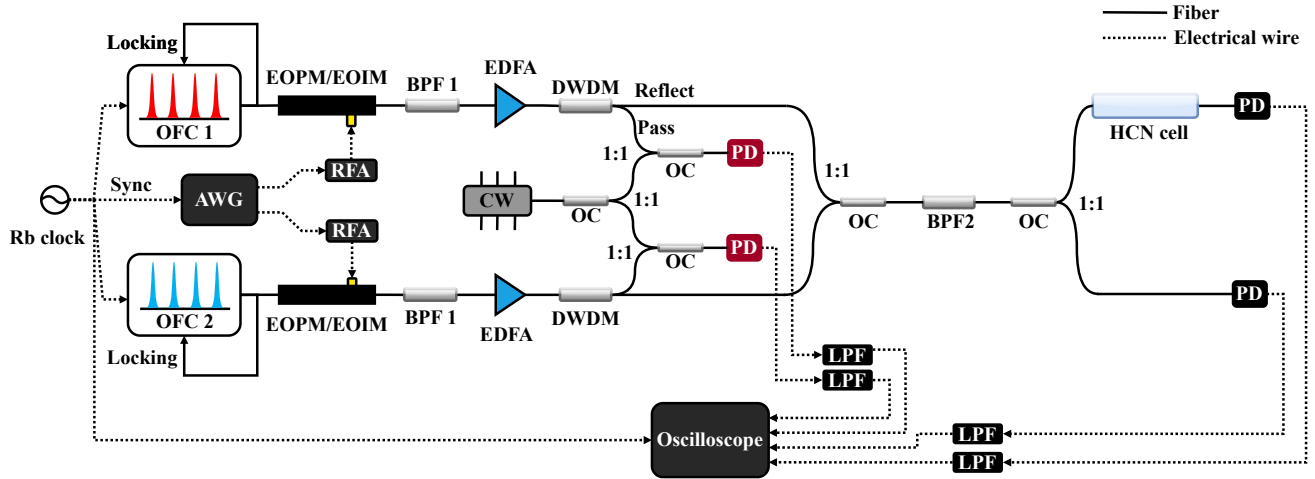


Fig. S1: Experimental setup. The DWDMs split every incident pulse trains into two beams; the two pass beams with a narrow band (1.3 nm@25 dB) are sent to beat against a CW on amplified detectors; the two reflect beam that contains the rest of spectrum are combined and then filtered by the tunable BPF 2 (0.3 nm@12 dB) to avoid spectrum aliasing of DCS. OFC: optical frequency comb, EOPM: electro-optic phase modulator, EOIM: electro-optic intensity modulator, AWG: arbitrary waveform generator, RFA: rf amplifier, BPF: band-pass filter, EDFA: erbium-doped fiber amplifier, CW: continuous wave laser, DWDM: dense wavelength-division multiplexing, OC: optical coupler, PD: photodetector, LPF: low-pass filter. The two pulse trains after modulation are pre-filtered by BPFs 1 (10 nm@25 dB) and amplified.

Figure S1 shows the detailed experimental setup. In hardware, a continuous wave (CW) laser is used as an intermediate oscillator to deploy the optical referencing technique and post-treatment, beating against one tooth from each of the two combs and generating two beat note signals that record the relative phase fluctuations between the CW laser and each tooth. When mixing the two beat note signals, the contribution of the CW is canceled and the resulting mixed signal contains only the relative phase fluctuations of the two comb teeth. Further mixing of the IGMs with this mixed signal pins this frequency component in the RF comb to DC¹. This effectively removes the absolute frequency offset, leaving only the spacing fluctuations relative to DC in the RF comb, which can then be solved by classical digital resampling, originally developed for FTIR. The true phase of the Δf_{rep} signal required for the resampling step is obtained by calculating the cross-correlation functions between the IGM stream^{2,3} to precisely locate the position of each centerburst, i.e., the position where the phase is $2n\pi$ and then interpolation. In addition, two common EDFAs containing approximately 1 meter of gain fiber, are employed to ensure that the IGMs of the C-DCS have enough

SNR to implement the cross-correlation function. Considering the trade-off between the complexity of the setup and the optical power, a single amplification stage was selected.

Notice that the noise tracking bandwidth for the Δf_{rep} signal by the cross-correlation function is a half of the centerburst repetition rate⁴. Therefore, in theory, the C-H-DCS obtains the best correction; however, we believe that this discrepancy does not have a substantial impact on the conclusions presented in the main text.

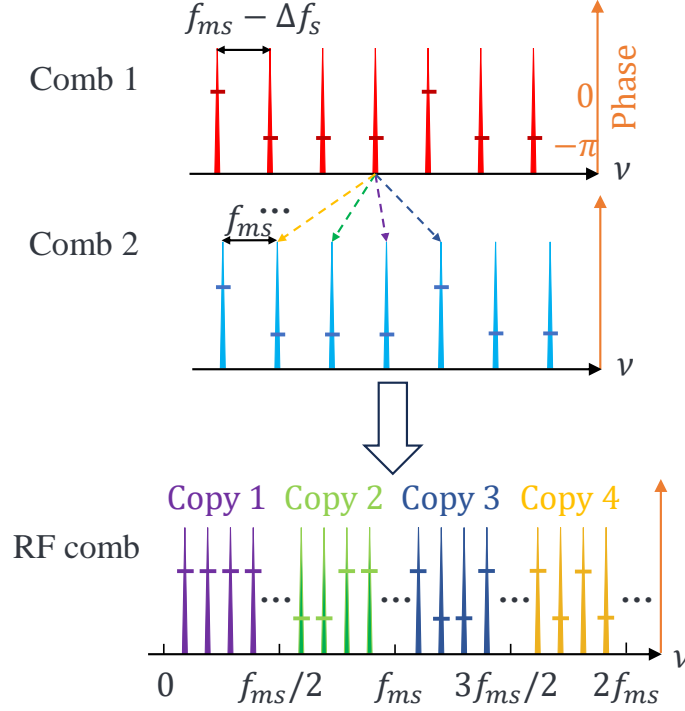


Fig. S2: Illustration of spectral copies generated by the heterodyning of teeth from comb 1 with non-nearest teeth from comb 2.

The higher-order components in the interferogram of H-H-DCS correspond to spectral copies on the spectrum, which are illustrated in Fig. S2. The different mode-phase profiles of these copies led to their self-imaging and time shift in the time domain. These properties are more evident when the two TPM signals are based on the quadratic forms of the "Talbot condition" (see Equ. 3). In that case, the phase profiles of these copies exhibit a linear dependence on the line number j :

$$\begin{aligned}\varphi_{j,h} &= \left(-\pi \frac{p}{m} j^2\right) - \left[-\pi \frac{p}{m} (j-h)^2\right] \\ &= -2\pi \frac{p}{m} h j + \pi \frac{p}{m} h^2,\end{aligned}\tag{S1}$$

where h denotes the detuning line number and belongs to the range $[-m/2, m/2]$. The first term, $-2\pi \frac{p}{m} h j$, mirrors the time-shift property of the Fourier transform, $\mathcal{F}\{f(t-t_0)\} = e^{-i2\pi j f_{\text{ms}} t_0} F(\omega)$, indicating a time shift $t_h = h \cdot \frac{p}{m f_{\text{ms}}}$ for these copies. The second term, $\pi \frac{p}{m} h^2$, signifies a carrier-envelope-phase (CEP) shift that varies with h , which does not impact the centerburst distribution. In a basic scenario with $p = 1$, the centerbursts corresponding to each copy are uniformly distributed across the interferogram within a period, spaced at intervals of $1/(m f_{\text{ms}})$. This conclusion holds true for any p setting, given that p and m are coprime and possess opposite parity, indicating that the interference electric fields associated with multiple copies are dispersed into m parts in the time domain, rather than being concentrated into a single centerburst as in C-DCS. Figure S3(a) shows the interferogram obtained during the H-H-DCS experiment when using a 125 MHz electronic low-pass filter, resulting in the inclusion of 20 spectral copies. The centerburst repetition rate is 20 kHz rather than 1 kHz, and each centerburst has a different carrier frequency.

These higher-order components can be further utilized to perform spectral-copy averaging to improve SNR, as demonstrated by M. Walsh et al⁵. The averaging method can be replaced by simply undersampling at a sampling

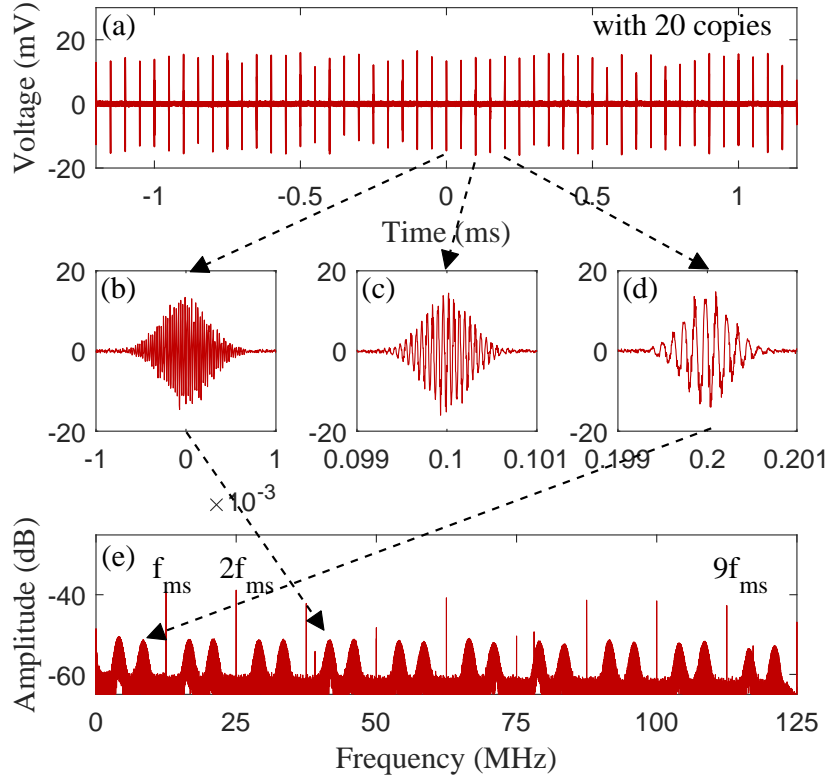


Fig. S3: (a) Interferograms of the H-H-DCS and (e) its spectrum with 20 spectral copies. The frequencies evenly spaced in the spectrum at intervals of 12.5 MHz are harmonics of the comb mode spacing. These harmonics have negligible impact on (a) interferograms due to their low amplitude and inconsistent phase. (b–d) Centerbursts corresponding to different spectral copies, show different carrier frequencies.

frequency of $f_{ms}/2$, in which case the characteristics of the resulting interferogram are expected to be the same as those in C-H-DCS.

-
- [1] Roy, J., Deschênes, J.-D., Potvin, S. & Genest, J. Continuous real-time correction and averaging for frequency comb interferometry. *Optics Express* **20**, 21932 (2012).
 - [2] Hébert, N. B. *et al.* Self-corrected chip-based dual-comb spectrometer. *Optics Express* **25**, 8168 (2017).
 - [3] Hébert, N. B. MATLAB Program Implementing the Self-Correction Algorithm. <https://www.mathworks.com/matlabcentral/fileexchange/69759-selfcorrectigns> (2019). Accessed: Dec, 23, 2024.
 - [4] Hébert, N. B., Michaud-Belleau, V., Deschenes, J.-D. & Genest, J. Self-Correction Limits in Dual-Comb Interferometry. *IEEE Journal of Quantum Electronics* **55**, 1–11 (2019).
 - [5] Walsh, M., Guay, P. & Genest, J. Unlocking a lower shot noise limit in dual-comb interferometry. *APL Photonics* **8**, 071302 (2023).